Peer-reviewed version available at *Aerospace* **2018**, *5*, 106; doi:10.3390/aerospace5040106

Article

A Multi-Scale Modeling Approach for Simulating Crack Sensing in Polymer Fibrous Composites Using Electrically Conductive Carbon Nanotube Networks. Part II: Meso- and Macro-Scale Analyses

Konstantinos Tserpes [1,*], Christos Kora [1]

[1] Laboratory of Technology & Strength of Materials, Department of Mechanical Engineering & Aeronautics, University of Patras, Patras, 26500, Greece

* Correspondence: kitserpes@upatras.gr

Abstract: This is the second of a two-paper series describing a multi-scale modeling approach developed to simulate crack sensing in polymer fibrous composites by exploiting interruption of electrically conductive carbon nanotube (CNT) networks. The approach is based on the finite element (FE) method. FE models at three different scales, namely the micro-scale, the meso-scale and the macro-scale, have been developed using the ANSYS PDL environment. In the present paper, the meso- and macro-scale analyses are described. In the meso-scale, a two-dimensional model of the CNT/polymer matrix reinforced by carbon fibers is used to develop a crack sensing methodology from a parametric study which relates the crack position and length with the reduction of current flow. In the meso-model, the effective electrical conductivity of the CNT/polymer computed from the micro-scale is used as input. In the macro-scale, the final implementation of the crack sensing methodology is performed on a CNT/polymer/carbon fiber composite volume using as input the electrical response of the cracked CNT/polymer derived at the micro-scale and the crack sensing methodology. Analyses have been performed for cracks of two different lengths. In both cases, the numerical model predicts with good accuracy both the length and position of the crack. These results highlight the prospect of conductive CNT networks to be used as a localized structural health monitoring technique.

Keywords: Carbon nanotubes; Polymer nanocomposites; Electrical conductivity; Crack sensing; Multi-scale modeling

1. Introduction

Structural Health Monitoring (SHM) aims to provide at every moment during the life of a structure, a diagnosis of the "integrity" of the constituent materials, of the different parts, and of the full structure. According to [1], an effective SHM system potentially minimizes the time for ground inspections, increases the availability of the aircraft and allows a reduction of the total maintenance cost by more than 30% for an aircraft fleet. These advantages represent a major contribution towards greener aviation. SHM is comprised from the diagnosis and prognosis functions. The diagnosis function is based on a monitoring system, which usually consists of a network of a limited number of sensors distributed over a relatively large area of the structure. However, with such a monitoring system only major damage conditions can be detected. The current trend is the development of dense wireless networks of miniaturized sensors. In addition, multifunctional materials for SHM have gained attention for their versatility to sense, actuate and harvest energy from ambient vibrations.

Combining extraordinary mechanical [2-5], thermal [6] and electrical properties [7] with fiber-like structure, CNTs are used as reinforcements to produce multifunctional polymers (nanocomposites) and fiber composites. Amongst the targeted functionalities is strain and damage sensing. Damage sensing in fiber composites by conductive CNT networks has been initially proposed by Fiedler et al [8]. Since then, numerous works, mainly experimental (e.g. [9-13]), have

Peer-reviewed version available at Aerospace 2018, 5, 106; doi:10.3390/aerospace5040106

been reported. On the contrary, there have been reported only two works on the modeling of damage sensing by CNT networks, one for fiber composites [11] and one for nanocomposites [12]. Li and Chou [11] modeled damage sensing in [0/90]s cross-ply glass fiber composites using embedded CNT network. The contact resistances of CNTs were modeled considering the electrical tunneling effect and the effective electrical resistance of the percolating nanotube network was calculated by considering nanotube matrix resistors and employing the finite element (FE) method for electrical circuits. The loading process of the composite, from initial loading to final failure, has been simulated also by the FE method. The deformation and damage induced resistance change has been identified at each loading step. The results demonstrated that the simulation model captures the essential parameters affecting the electrical resistance of nanotube networks. The authors did not carry out any parametric study. Kuronuma et al. [12] presented an analytical model of strain sensing behavior of CNT-based nanocomposites. The model incorporated the electrical tunneling effect due to the matrix material between CNTs to describe the electrical resistance change as a result of mechanical deformation. The model deals with the inter-nanotube matrix deformation at the micro/nanoscale due to the macroscale deformation of the nanocomposites. A comparison of the analytical predictions with the experimental data showed that the proposed model captures the sensing behavior.

From the above, we conclude that the understanding of the key factors governing the sensing effectiveness of CNT networks has been mainly attempted by experimental means. However, in this process, reliable models and simulation-driven design tools could be very useful as they are cost and time-effective. In this context, in the present work proposed is a multi-scale FE-based modeling approach for simulating the basic mechanisms of crack sensing by conductive CNT networks in polymers and fibrous composites. The modeling approach is described in two papers. The first paper [13] describes the micro-scale model. The present paper describes the development of a crack sensing methodology by means of a meso-scale model and a parametric study and the final implementation of the crack sensing methodology for predicting the length and position of cracks at the macro-scale.

2. Meso-scale model

2.1. Geometry and FE model

In the meso-scale, a 2D model of a CNT/polymer reinforced by carbon fibers has been developed. The modeled area is a transverse section of size of 0.2 mm ⊚ 0.2 mm containing 400 fibers (circular cross-sections). The fibers are placed in a square configuration, but they are not equally spaced. The aim of this analysis is to develop a crack sensing methodology through the parametric correlation of current drop with the characteristics of the crack (length and position). The analysis is based on the simplicity of the implementation of the DC current for measuring the variation of resistance in conductive composites (e.g. the four-probe method e.g. [9]) and the through-the-thickness measurement of resistance in thin-walled structures with a known transverse conductivity. Both the fibers and the matrix are modeled using the ANSYS PLANE223 triangular elements [14]. The 3-node option of the elements has been used as it was found that reduces significantly the computational effort without compromising considerably the accuracy of the results. The FE mesh of the meso-scale model is shown in Figure 1.

For the transition to the meso-scale, we consider electrically homogeneous matrix and a full bonding between the fibers and the matrix. To model the presence of CNTs in the matrix, values of the effective electrical conductivity above the percolation threshold as derived from the micro-scale, are assigned to the elements of the model.

Preprints (www.preprints.org) | NOT PEER-REVIEWED | Posted: 27 August 2018 doi:10.20944/preprints201808.0456.v1

Peer-reviewed version available at Aerospace 2018, 5, 106; doi:10.3390/aerospace5040106

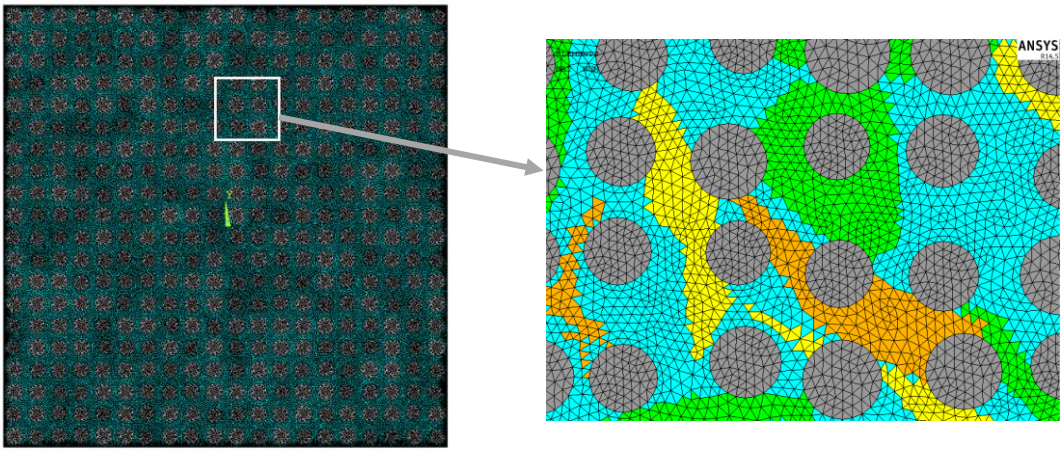

Figure 1. FE mesh of the meso-scale model

2.2. Charging

Charging has been applied to the model using a series of circuit elements (ANSYS CIRCU124 elements [14]) placed at the top nodes. These are 2-node circuit elements with a constant resistance which are not affected by geometrical factors. The contact with the upper end of the model is utilized using common nodes. A circuit element was placed at each node of the plane elements. A voltage V_0 is applied to the free node of the circuit element while the lower nodes of the model are grounded. A benefit from the use of circuit elements is the direct computation of reaction currents without the need for gathering and processing data from the interior of the model.

The sketch in Figure 2 describes the simple electric circuit of the meso-scale model. The reaction current i_R is simply derived from the Ohm's law as

$$i_R = \frac{V_0}{R_0 + R_p}, \tag{1}$$

where V_0 is the voltage and R_0 and R_p are the resistances. Furthermore, the parallel network of the circuit elements provides information about the location of the current drop.

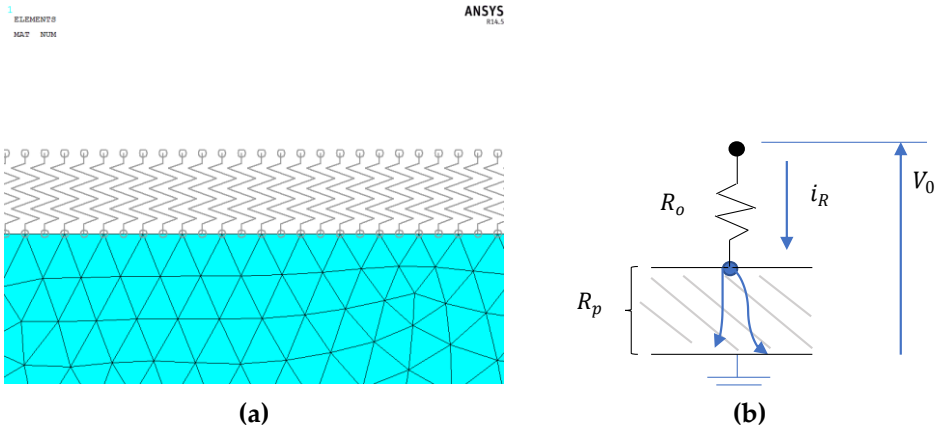

Figure 2. (a) Part of the FE mesh of the meso-scale model showing the connection of the circuit elements with the nodes of the nanocomposite and (b) Sketch of the electric circuit of the meso-scale model

2.3. Crack sensing methodology

The proposed crack sensing methodology is based on the parameterization of the measurements derived for different crack lengths and crack distance from the measurement points (crack depth). It is assumed that the crack is single, continuous and parallel to the x axis. Inclined cracks might be also

Preprints (www.preprints.org) | NOT PEER-REVIEWED | Posted: 27 August 2018 doi:10.20944/preprints201808.0456.v1

Peer-reviewed version available at Aerospace 2018, 5, 106; doi:10.3390/aerospace5040106

considered by using the effective length, which is projection of the inclined crack to the x direction. The crack is introduced in the mesh by releasing nodes as it was done in the micro-scale model.

For each crack case, we derive through repetitive analyses the reaction currents $i_R^{i,l,d}$) at the circuit elements (*i* is the number of circuit element, *l* is the crack length and *d* is the crack depth. For a constant depth, we derive the reaction current for different crack lengths and we compare the values with the reference value of the uncracked material $i_R^{i,0}$). This way, we evaluate the effect of crack length on the current drop for each circuit through the current drop parameter $\delta i_R^{i,l,d}$ given by

$$\delta I_R^{i,l,d} = \frac{I_R^{i,0} - I_R^{i,l,d}}{I_R^{i,0}} \times 100\%, \tag{2}$$

Figure 3 shows a typical computed distribution of current drop around the crack zone. It is observed that outside the crack zone the reaction current increases (negative $\delta i_R^{i,l,d}$) due to the redistribution of current flow in the area around the crack. As shown, the maximum current drop occurs at the centroid of the crack. Using the electrical response of the reference material we define in the diagram the maximum current drop value (*drop*) and the difference between the maximum and minimum current drops (*span*). The latter was used to quantify the inhomogeneity of the electrical response, i.e. whether a sudden or a smooth increase takes place. For the difference between the maximum and minimum current drops to be generalized, span is normalized over the maximum current *drop* value. Based on the above, we have

$$drop = \max(\delta I_R^{i,l,d}), \tag{3}$$

$$span = \frac{\max(\delta I_R^{i,l,d}) - \min(\delta I_R^{i,l,d})}{\max(\delta I_R^{i,l,d})}, \tag{4}$$

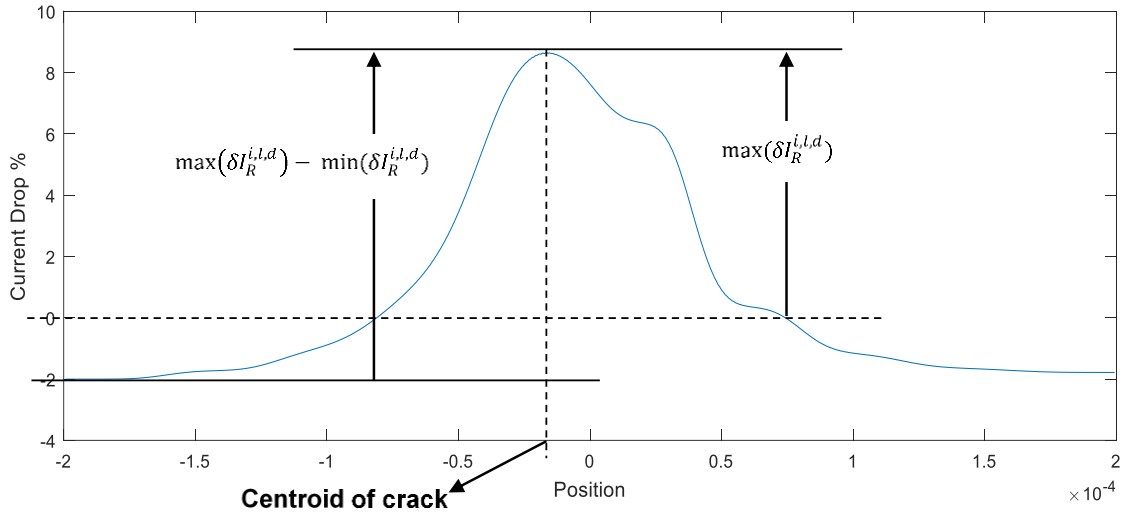

Figure 3. An example of the electrical response curve in the area around the crack.

A parametric study has been performed to correlate the different crack scenarios with the measured values of the *drop* and span values and develop generalized functions. By cross-checking the drop and *span* values for every circuit element, the maximum values are located. Then, 2D plots of the maximum values with regards to the normalized crack length and normalized crack depth are created and every surface is fitted with a two-variable function. The outcome of this process, when compared to the outcome of the reference material can give an estimation about the size and location

of the crack. Graphically, this can be implemented by using the cross-section of the curves derived from the cross-section of the *drop* and *span* surface plots.

3. Macro-scale model

3.1. Geometry and FE modeling

In the macro-scale, a CNT/polymer/carbon fibers composite volume of dimensions of 10 mm × 10 mm × 2.5 mm has been modeled. The volume has been meshed with 20-node SOLID131 elements [14]. The mesh density is selected such as each element to have the dimensions of the micro-model. The FE mesh of the macro-model is shown in Figure 4. The effective electrical conductivity derived from the micro-scale is assigned to each element. Despite the considered CNT volume fraction is well above the percolation threshold ($V_f = 0.04\%$), the inhomogeneous electrical conductivity due to the inhomogeneous CNT network has been simulated by randomly varying the effective electrical conductivity of the elements. To this end, the random numbers functions of the ANSYS FE code were used. The electrical conductivity of the solid elements in the fibers direction has been computed using the rule of mixtures:

$$\sigma_z = \sigma_{fib} \times 0.55 + \sigma_m \times 0.45 \quad (5)$$

where σ_{fib} is the conductivity of the fibers and σ_m is the conductivity of the matrix.

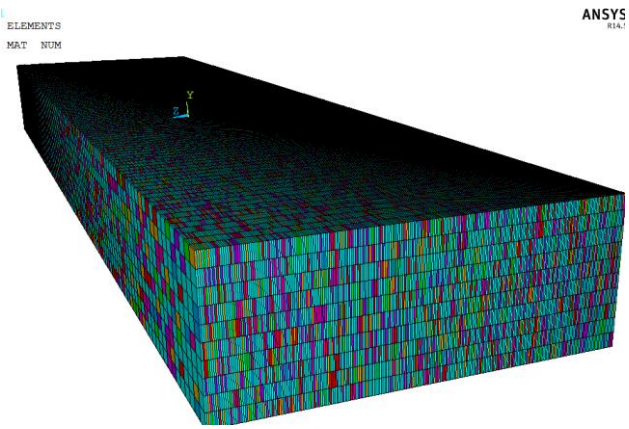

Figure 4. FE mesh of the macro-scale model

3.2. Introduction of a virtual crack, charging and computations

As for the meso-scale model, charging has been applied to the macro-scale model using circuit elements CIRCUIT124 [13] which are placed on the nodes of the top *XY* surface while the nodes of the bottom surface are grounded. Crack growth in the composite volume has been simulated by applying the corresponding drop of effective conductivity σ_{eff} at the elements of crack path using the micro-scale analysis results on the variation of σ_{eff} with regards to crack length. Computations have been performed by gathering the values of the current from the circuit elements and comparing them with the corresponding values of the reference model. Then, the differences are qualified on the plane, thus producing a graphical representation for the location and magnitude of the current drop at the *XY* plane. In order to validate the meso-scale model, results from the macro-scale for a known crack have been used.

4. Numerical results

4.1. Meso-scale: Effect of crack presence

Preprints (www.preprints.org) | NOT PEER-REVIEWED | Posted: 27 August 2018 doi:10.20944/preprints201808.0456.v1

Peer-reviewed version available at Aerospace 2018, 5, 106; doi:10.3390/aerospace5040106

In the meso-scale, the electrical response of models with 39 different crack lengths and 9 different depths has been simulated. Crack length and depth are normalized with regards to the dimension of the RVE, $l_0 = 0.2\,\text{mm}$. The input parameters and material properties of the meso-scale model are listed in Table 1. Note that the resistance of the circuit elements does not affect the results.

Table 1. Input parameters and materials properties in the macro-scale model

Parameter/Property	Value
Fiber's diameter	6-8 μm
Fiber volume fraction	55%
Fiber's electrical conductivity at Υ direction, σ_{cf}^{y}	1e4 S/m
Fiber's electrical conductivity at X direction, σ_{cf}^{x}	1e4 S/m
Electrical conductivity of polymeric matrix, σ_m $V_{fCNT} = 0.2\%$	1e-3 S/m
Electrical resistance of circuit elements	1e3 Ohm

The predicted drop and span values for the different l_c / l_0 and d / l_0 ratios have been listed in tables. Table 2 lists the results for the case of $d / l_0 = -0.1$. The other tables are omitted for the sake of briefness. To visualize the data, 3D plots have been created from tabular data in the Matlab software using fitting functions. Figure 5 shows the 3D plot of drop vs. l_c / l_0 and d / l_0 for the maximum drop while Figure 6 shows the 3D plot of span vs. l_c / l_0 and d / l_0 for the maximum span. We observe a decrease in the sensitivity of the response with increasing the depth ratio d / l_0.

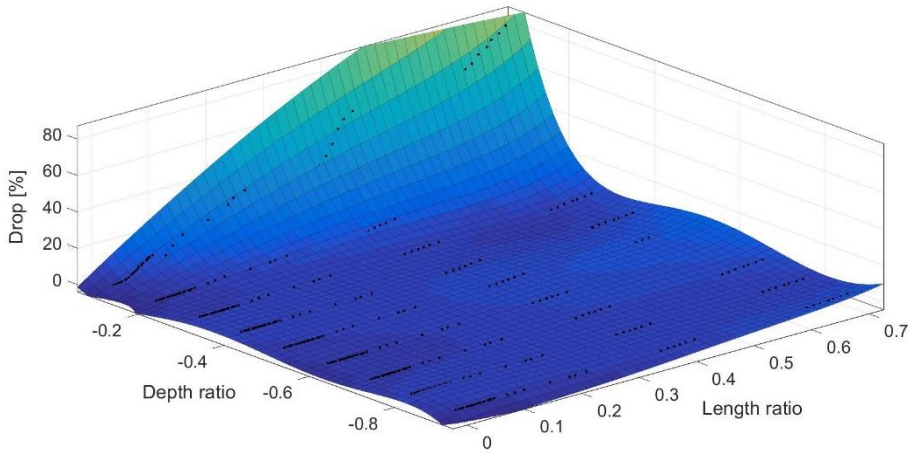

Figure 5. Fitted 3D plot of the *drop* function with regards to length ratio l_c / l_0 and depth ratio d / l_0

Preprints (www.preprints.org) | NOT PEER-REVIEWED | Posted: 27 August 2018 doi:10.20944/preprints201808.0456.v1

Peer-reviewed version available at Aerospace 2018, 5, 106; doi:10.3390/aerospace5040106

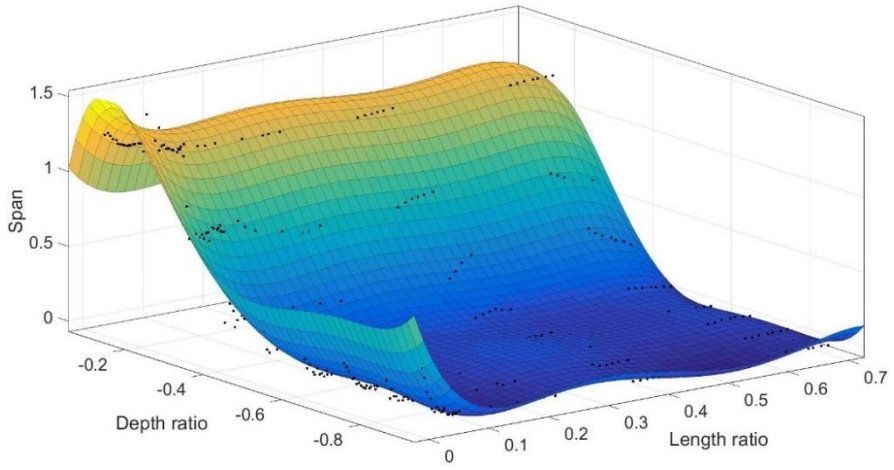

Figure 6. Fitted 3D plot of the *span* function with regards to length ratio l_c / l_0 and depth ratio d / l_0

Table 2. *drop* and *span* values vs. length ratio, l_c / l_0 and depth ratio $d / l_0 = -0.1$

Length ratio, l_c / l_0	*drop* [%]	*span*
0.00944267050000000	0.376322286095307	1.25186375445180
0.0148023080000000	0.425734043444282	1.26144516747466
0.0188990450000000	0.628888774067786	1.23809785726492
0.0230416450000000	0.762768551621184	1.21390147841638
0.0291938930000000	1.32767604821474	1.20286058578767
0.0313924080000000	1.72355562344860	1.17707741001034
0.0357894380000000	2.17836238080806	1.17026823569497
0.0399052110000000	3.34286531042766	1.16364174309429
0.0431978300000000	3.83183270857989	1.15717578538481
0.0472043000000000	4.50758833772322	1.15117431085395
0.0504094760000000	5.24997187084398	1.15204159696837
0.0522886180000000	6.45652024117642	1.15207792088315
0.0572900860000000	7.01241419089021	1.15298495797038
0.0595954400000000	7.85039799968788	1.15311959265536
0.0658174630000000	8.79396173883472	1.15349676433320
0.0674460530000000	9.34543875498501	1.15198640708327
0.0704260440000000	9.89706496377527	1.14971675557009
0.0715739230000000	10.1524333911046	1.14934200514836
0.0768762850000000	10.6413313750063	1.14757722793076
0.100000000000000	8.64427956441889	1.23175612986261
0.112308550000000	12.9222701873760	1.20756986327765
0.129010120000000	17.3962482573007	1.19253403777262
0.173799290000000	21.6637854439888	1.18118638731867
0.208353730000000	27.0841020761326	1.17016338908504
0.217732150000000	29.9100284804437	1.16553394669254
0.237302020000000	32.3452443856801	1.16232055408389
0.366945250000000	35.6776420549543	1.15899930903691

Preprints (www.preprints.org) | NOT PEER-REVIEWED | Posted: 27 August 2018 doi:10.20944/preprints201808.0456.v1

Peer-reviewed version available at Aerospace 2018, 5, 106; doi:10.3390/aerospace5040106

0.379235750000000	38.6929920506905	1.15691754446509
0.390348750000000	44.4116592560641	1.15482288498663
0.400104170000000	51.9034953962641	1.15120520717196
0.410234770000000	56.3780492624871	1.14863642195611
0.425741150000000	59.3756186810118	1.14688600623077
0.622028600000000	65.2634979785141	1.14360376860245
0.633392100000000	67.2295772156926	1.14218233276664
0.644763470000000	71.4113850270268	1.14134066208636
0.659507550000000	74.1125263423852	1.14127150930764
0.667182170000000	77.3643759768323	1.14157795043898
0.680908500000000	79.7455425784586	1.14289340353258
0.692418130000000	83.0531238703329	1.14595668362933

To implement the opposite procedure, i.e. the characterization of a cracked model, we assume random values of drop and span and through the intersection of the 3D plots we derive the l_c / l_0 and d / l_0 ratios, which describe the length and location of the crack. For instance, for *drop* = 6.2% and *span* = 1.18%, we obtain the projection-curves (black lines) in the 3D plots shown in Figs. 7 and 8, respectively. Combining the two projection-curves, as shown in Figure 9, we obtain two common solutions at the intersections of the curves. The selection of a unique solution requires more data. However, if we use the solution with the maximum l_c / l_0 ratio, i.e. $l_c / l_0 = 0.28$ and $d / l_0 = -0.21$, we get a crack length of $l_c = 0.056$ mm and a depth of $d = 0.042$ mm.

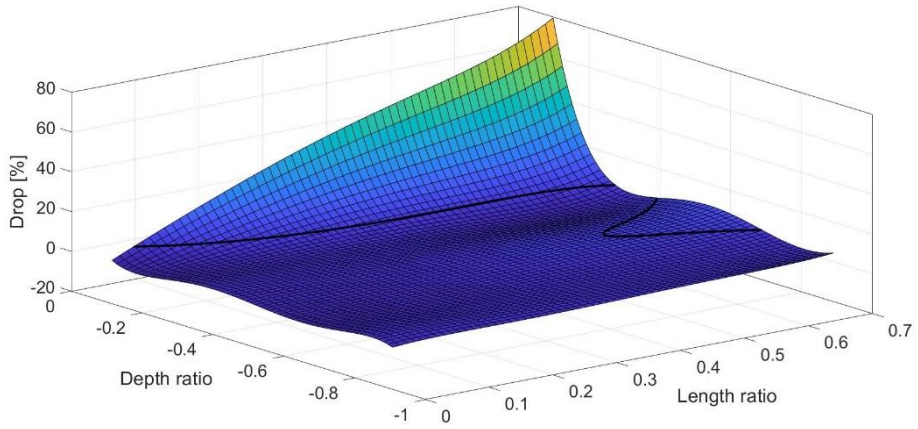

Figure 7. Intersection curve for *drop* = 6.2%

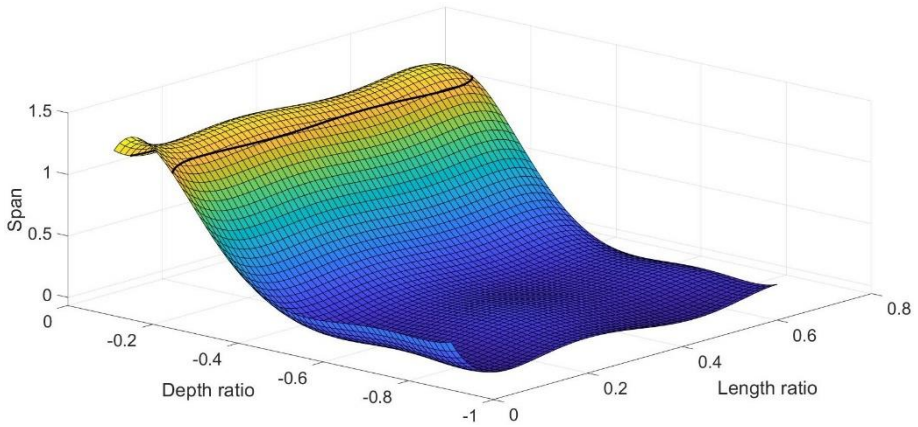

Figure 8. Intersection curve for *span* = 1.18%

Preprints (www.preprints.org) | NOT PEER-REVIEWED | Posted: 27 August 2018 doi:10.20944/preprints201808.0456.v1

Peer-reviewed version available at Aerospace 2018, 5, 106; doi:10.3390/aerospace5040106

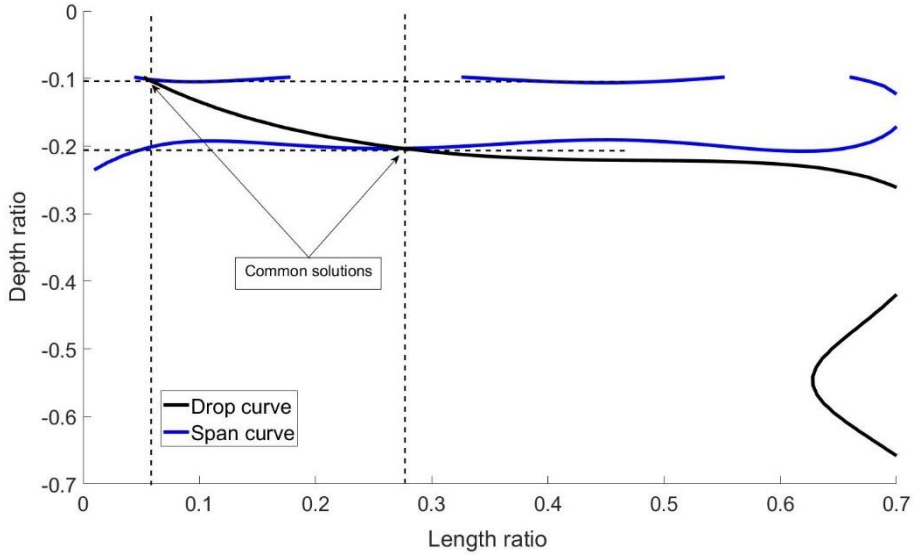

Figure 9. Intersection curves for *drop* = 6.2% and *span* = 1.18%

4.2. Macro-scale: Crack detection

The input parameters and material properties of the macro-scale model are listed in Table 3. In the macro-scale, we examine the model's capability of detecting a crack in the *ZY* plane introduced through the reduction of element's electrical conductivity derived from the micro-scale analysis [14]. Two cracks (crack1 and (crack2) of different length have been modeled at the same location; their characteristics are listed in Table 4.

Table 3. Input parameters and materials properties in the macro-scale model

Parameter/Property	**Value**
Fiber volume fraction	55%
Range of transverse conductivity	1e-4 – 1e-2 S/m
Fiber's electrical conductivity at *Z* direction, σ_{cf}^{z}	1e5 S/m
Electrical resistance of circuit elements	1e3 Ohm

Table 4. The characteristics of the cracks modeled

	Position (*X*, *Z*) [mm]	**Depth from top surface [mm]**	**Length [μm]**	**Reduction in [%]**
1	(6,2)	-0.2	50 μm	59
2	(6,2)	-0.2	100 μm	100

By comparing the current values taken from the circuit elements for the reference and the cracked model, we plot the results at the *XZ* plane in Figure 9. The obtained inhomogeneity of the current distribution is due to the inhomogeneous electrical properties of the model's elements.

The computed contours of *drop* at the *Y* direction due to the presence of crack1 and crack2 are plotted on the *XZ* plane in Figures 10 and 11, respectively. The results have been normalized by the current of the reference model. As shown, in both cases the location of the current drop at the *Y* direction matches the location of the crack. For crack1, given the crack spans through the width of the modified element, the ratio of the crack surface to the XZ surface of the model is $\frac{50\ \mu\text{m}\times 10\ \mu\text{m}}{1e4\ \mu\text{m}\times 2.5e3\mu\text{m}} = 0.00002 = 0.002\%$. Hence, the response is quite large compared to the

modeled crack length. The reason for choosing the width of 0.2 mm (20% of the model's width) is because the meso-scale analyses have shown that smaller crack widths give very weak responses. In the case of crack2, the magnitude of electrical response increases by 643.3% for a 100% increase in crack length from 50 μm to 100 μm. This finding is an indication of the high sensitivity of the model to the crack length.

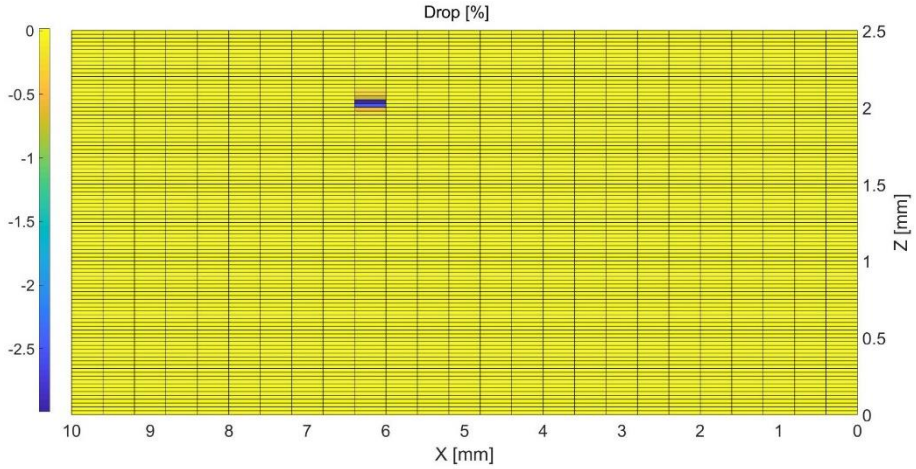

Figure 10. 2D plot of the drop at the XZ plane for crack1 (50 μm).

To further exploit the above findings, we note that the same technique does not have the same sensitivity in metallic materials since in that case the electric current from the cracked area is redistributed to the remaining material volume and the *drop* is not detectable. On the contrary, due to the very small volume of the CNT network compared to the volume of the composite material, any interruption of the network, which leads to the redistribution of electric current, is detectable.

Aiming to characterize crack1, we use the technique described in the previous section. Based on the computed values of drop and span, we delimit the area around the crack until the nodes where the electrical response is fully recovered (zero value). The dimension of the perturbation area is defined as the dimension in the direction of the denser mesh (Z direction). For crack1, we define an area of dimension of 250 μm and for this area we read *drop* = 3% and *span* = 1.1. The intersection of the drop and span intersection-curves shown in Figure 12 gives a length ratio of 2.1, a crack length of 52.5 μm and a depth ratio of -1.88. The characterized values of crack length and crack depth are close to the actual values, something which validates the proposed crack sensing methodology.

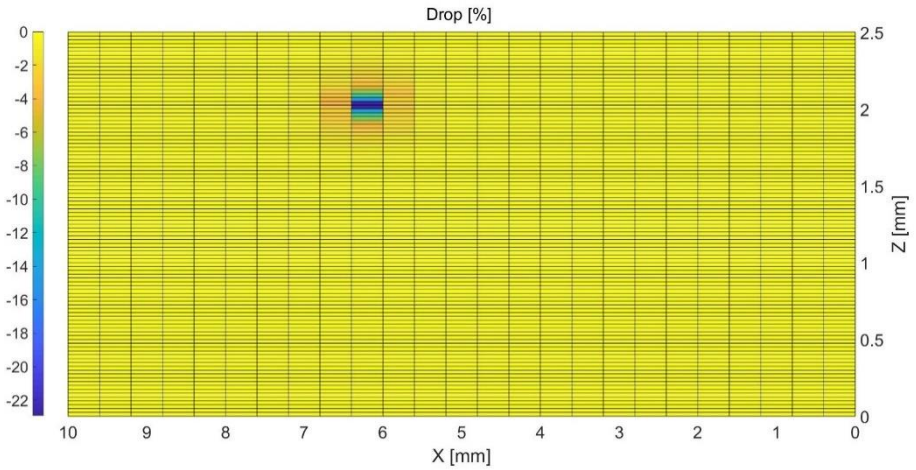

Figure 11. 2D plot of the drop at the XZ plane for crack1 (100 μm).

Peer-reviewed version available at Aerospace 2018, 5, 106; doi:10.3390/aerospace5040106

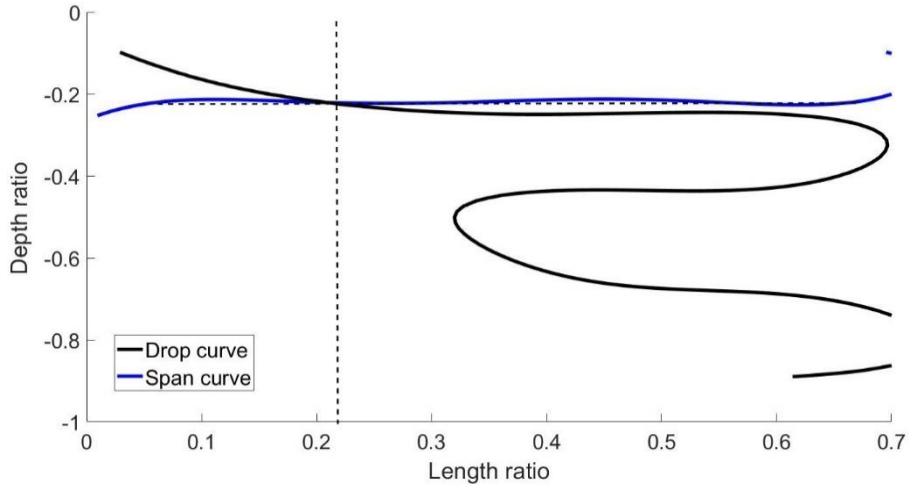

Figure 12. Intersection curves for *drop* = 1.1% and *span* = 1.18%

5. Conclusions

This is the second of a two-paper series describing a multi-scale modeling approach developed to simulate crack sensing in polymer fibrous composites by exploiting interruption of electrically conductive carbon nanotube (CNT) networks. In the present paper, the meso- and macro-scale analyses has been described. In the meso-scale, a crack sensing methodology has been developed by means of a parametric study which correlates the crack characteristics with the current drop characteristics. In the macro-scale, the final implementation of the crack sensing methodology has been made for cracks of different lengths. The numerical results show a large sensitivity of the current flow to the crack length. Moreover, the model has been proved capable of predicting both the length and the position of the cracks considered.

Based on the findings of the two papers, we can conclude that the proposed multi-scale electrical modeling approach is capable of simulating the electrical response of CNT/polymers and CNT/composites. The model in combination with the crack sensing methodology is also capable of characterizing cracks in these materials. The proposed modeling approach after being improved could be used for the virtual design and optimization of structural health monitoring systems based on conductive CNT networks in polymers, epoxy adhesives and polymer fibrous composites.

Acknowledgement

Part of the work reported in this paper has received funding from the European Union's Horizon 2020 research and innovation programme ECO-COMPASS (Grant no. 690638).

References

1. Boller, C. Why SHM? A Motivation, NATO Lecture Series STO-MP-AVT-220 Structural Health Monitoring of Military Vehicles: STO Educational Notes **2014**.
2. Tserpes, K.I.; Papanikos, P. Finite element modeling of single-walled carbon nanotubes, *Compos Part B Eng*. **2005**, 36, 468-477, https://doi.org/10.1016/j.compositesb.2004.10.003.
3. Papanikos, P; Nikolopoulos, D.D.; Tserpes, K.I. Equivalent beams for carbon nanotubes. *Computational Materials Science*, **2008**, 43, 345-352, https://doi.org/10.1016/j.commatsci.2007.12.010.
4. Tserpes, K.I.; Papanikos, P; Tsirkas, S.A. A progressive fracture model for carbon nanotubes. *Compos Part B Eng*., **2006**, 37, 662-669, https://doi.org/10.1016/j.compositesb.2006.02.024.
5. Tserpes, K.I.; Papanikos, P. The effect of Stone–Wales defect on the tensile behavior and fracture of single-walled carbon nanotubes. *Compos Struct*, **2007**, 79, 581–589, https://doi.org/10.1016/j.compstruct.2006.02.020.
6. Kim, P.; Shi, L.; Majumdar, A. Mc Euen, P.L. Thermal transport measurements of individual multiwalled nanotube. *Phys Rev Lett*, **2001**, 87, 215502, DOI: 10.1103/PhysRevLett.87.215502.

7. Ebbesen, T.W. et al. Electrical conductivity of individual carbon nanotubes. *Nature*, **1996**, 382, 54–56, https://doi.org/10.1038/382054a0.
8. Fiedler, B. et al. Can carbon nanotubes be used to sense damage in composites? *Ann Chim-Sci Mat*, **2004**, 29, 81–94, https://doi.org/10.1088/0964-1726/23/7/075008.
9. Gallo, G.J; Thostenson, E.T. Electrical characterization and modeling of carbon nanotube and carbon fiber self-sensing composites for enhanced sensing of microcracks. *Materials Today Communications*, **2015**, 3, 17–26, https://doi.org/10.1016/j.mtcomm.2015.01.009.
10. Aly, K.; Li, A.; Bradford, P.D. Strain sensing in composites using aligned carbon nanotube sheets embedded in the interlaminar region. *Composites Part A: Applied Science and Manufacturing*, **2016**, 90, 536-548, https://doi.org/10.1016/j.compositesa.2016.08.003.
11. Li, C.; Chou, T-W. Modeling of damage sensing in fiber composites using carbon nanotube networks. *Composites Science and Technology*, 2008, 68, 3373–3379, https://doi.org/10.1016/j.compscitech.2008.09.025.
12. Kuronuma, Y. et al. Electrical resistance-based strain sensing in carbon nanotube/polymer composites under tension: Analytical modeling and experiments. *Composites Science and Technology*, **2012**, 72, 1678–1682, https://doi.org/10.1016/j.compscitech.2012.07.001.
13. Tserpes, K.; Kora, Ch. A multi-scale modeling approach for simulating crack sensing in polymer fibrous composites using electrically conductive carbon nanotube networks. Part II: Micro-scale analysis *Computational Materials Science* **2018**, 154, 530-537, https://doi.org/10.1016/j.commatsci.2018.07.048.
14. ANSYS User's manual, Version 11, Swanson Analysis Systems, 2008, Pittsburgh, PA, USA.